IEEE Access
Multidisciplinary | Rapid Review | Open Access Journal

Received June 24, 2020, accepted July 8, 2020, date of publication July 13, 2020, date of current version July 22, 2020.

Digital Object Identifier 10.1109/ACCESS.2020.3008690

Design of Navigation System for Liver Surgery Guided by Augmented Reality

FENGFENG ZHANG[1,2], (Member, IEEE), SHI ZHANG[3], KAI ZHONG[3], LINGTAO YU[3], AND LI NING SUN[1,2]

[1]School of Mechanical and Electrical Engineering, Soochow University, Suzhou 215006, China
[2]Collaborative Innovation Center of Suzhou Nano Science and Technology, Soochow University, Suzhou 215123, China
[3]College of Mechanical and Electrical Engineering, Harbin Engineering University, Harbin 150001, China

Corresponding author: Fengfeng Zhang (zhangfengfeng@suda.edu.cn)

This work was supported in part by the National Key Research and Development Project under Grant 2018YFB1307700.

ABSTRACT The traditional surgical navigation system combining preoperative CT and intraoperative ultrasound is widely used in open hepatectomy, but the problem of this system is that there are some errors in terms of the precision of the time and the space during the surgery. In order to solve the above problems, this paper introduces augmented reality technology into the surgical navigation system. In order to accurately describe the biomechanical characteristics of the liver and let the navigation system perform more accurately, this paper uses Tetgen to perform tetrahedral partition on the triangle mesh data obtained after the three-dimensional CT was reconstructed, and then the surface mesh data and the internal tetrahedral data were obtained and they were used to describe a whole liver model. The surface triangle mesh data is used to render graphics and describe the surface topology change, and the internal tetrahedral data combined with mass-spring theory is used to simulate deformation. Subsequently, the ex vivo pig liver was used to experimentally verify the accuracy of gravity deformation of the liver model, and the results show that the error was mainly distributed between -2mm and -2.5mm. At the same time, this paper uses the NDI Polaris infrared tracking system to carry out precision experiments on the augmented reality module, and the measured error is 1.55±0.29mm. Finally, various modules of the system are integrated to finish the experiment in which the ring-shaped lesions are cut from the ex vivo pig liver with the aid of augmented reality. The experimental error is 0±1.26mm, and with the assistance of the general purpose graphics processing unit (GPGPU), the refresh rate is above 200FPS. The results prove that the liver surgery navigation system proposed in this paper is excellent in terms of real-time performance and accuracy, which can help doctors accurately locate the tumor during surgery and perform ideal resection.

INDEX TERMS Open hepatectomy, augmented reality, liver model, mass-spring, surgical navigation system.

I. INTRODUCTION

In current liver surgery, partial hepatectomy is the golden standard method to avoid cancer metastasis and death [1]. However, the tissue structure inside the liver cannot be directly observed by the doctor during the operation, which means that the doctor cannot locate the lesion precisely during the operation [2].

In order to solve the above problems, an effective method is to use the surgical navigation system as an auxiliary tool, and then help the doctor to obtain needed information [3]. Traditional surgical navigation systems use ultrasound, MRI, or patient pre-operative CT and other medical images to provide doctors with reference information [4]. However, in this process, the doctor needs to connect the two-dimensional image with the three-dimensional space, which will cause the problem of mismatch between preoperative CT and intraoperative information. In addition, CT and MRI can only be separated by interval imaging. And the quality of ultrasound imaging is poor. As the result of these causes, the accuracy of surgical navigation will not reach a satisfactory level. At the same time, when using a traditional surgical navigation system to perform surgery, the doctor needs to constantly switch the line of sight between the surgical scene and the auxiliary display, which will inevitably extend the operation time [5].

The introduction of augmented reality navigation systems, including video-based, projection-based and

The associate editor coordinating the review of this manuscript and approving it for publication was Jenny Mahoney.

perspective-based, can effectively solve the drawbacks of traditional surgical navigation systems [6]. During the operation, augmented reality technology can fuse the preoperative model with the intraoperative scene to provide doctors with real-time lesion information and surgical guidance [7], [8]. Up to now, augmented reality technology has been widely used in many fields, such as neurosurgery, orthopedic surgery, otolaryngological surgery, oral surgery and laparoscopic surgery [9]–[18]. However, in liver cutting surgery, whether it is laparoscopic surgery or open surgery, still greater efforts are needed in the application of augmented reality technology in the clinic. In the process of literature review of the author team, there are no more than 20 cases of liver surgery navigation system based on augmented reality.

Ntourakis *et al.* (2015) [19] proposed an augmented reality navigation system that implements registration based on the external anatomical structure of the liver, which combines virtual and real images in the video stream. The system was tested on 3 patients, and the results proved that the accuracy was maintained at 5mm. Pessaux *et al.* (2015) [20] adopted the same idea, manually fusing virtual and real images in the video, and finally used the navigation system in robotic hepatectomy. Okamoto *et al.* (2013) [21] used optical sensors to register internal organs and preoperative CT data, and used the system in the laparotomy for gallbladder cancer patients and liver cancer patients. The results prove that the system has a certain navigation effect for laparotomy, but many efforts still need to be made in the clinical trial stage. Rucker *et al.* (2014) [22] used intraoperative sparse data and pre-reconstructed models for registration, and used five deformed data sets for non-rigid registration, with an average error of 3.3mm. Adagolodjo *et al.* (2018) [23] proposed an identification-based method to track liver deformation during surgery. The marking point is manually attached to the surface of the liver after laparotomy, and is tracked in real time by an infrared camera during the subsequent surgery. The system has achieved considerable effects in vivo experiments. However, the infrared reflective markers in the surgical process are easily affected by the surgical environment (for example, bleeding), resulting in a decrease of registration accuracy. To this end, the team placed an active depth sensor above the patient's abdomen to complete an unmarked solution, which confirmed that after less than 10 minutes of configuration, it can achieve registration accuracy of 7.9 mm [24].

Because in liver resection surgery, open surgery has a wider field of view, and is more conducive to surgery when dealing with more complicated bile duct and blood vessel lesions. In this article, we propose an augmented reality-based initial surgical navigation system for open surgical procedures. The system registers liver and surgical instruments separately through identification, and its cutting accuracy and system operating efficiency are verified by the pig liver lesion cutting experiment. It is worth noting that the system can significantly improve the surgical accuracy and reduce the surgical time by registering the virtual model and the real model.

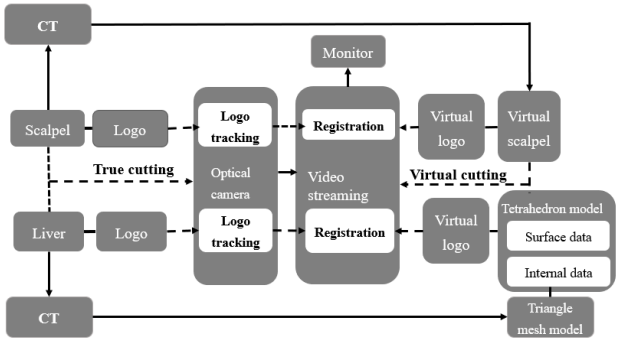

FIGURE 1. Overall framework of the liver cutting system.

II. OVERALL DESIGN OF THE EXPERIMENTAL PLATFORM

The overall framework of the system is shown in Figure 1. Before the cutting, CT scans of the liver and cutting tools were performed to obtain CT data of the liver and cutting tools, and then used the moving cube algorithm (MC) to three-dimensional reconstruction of CT to obtain a three-dimensional mesh model of liver and cutting tools. The calculation of the deformation of the liver during cutting requires the use of a tetrahedron model. In this paper, Tetgen is used to divide the liver model into tetrahedrons to obtain tetrahedral meshes. The tetrahedral meshes (the volume model) are used to calculate the deformation of the liver model. The three-dimensional mesh model (the surface model) is mainly used to calculate the topological change of the liver model when it is cut and to render display. The depth camera in the system is used to capture the video of the real cut on the one hand and to track the logo on the other hand, during the cutting process, the relative positions of the cutting tool and the liver with the corresponding markers are respectively fixed, and the virtual cutting tool and the virtual liver are also respectively fixed with corresponding virtual markers. The corresponding identification and model are registered in the video stream collected by the depth camera. At this time, when cutting in the real scene, virtual cutting will be performed in the virtual scene, and finally the fusion video of the augmented reality will be displayed.

A. SYSTEM HARDWARE

As shown in Figure 2, the system hardware consists of a cutting platform, a graphics workstation, a depth camera, and an NDI Polaris infrared tracking system. The cutting platform is formed by splicing the connecting members of the profile.

In order to control the deformation of the liver during cutting, and to ensure that the liver and the scalpel can be fixed relatively to the mark, a limiting device is designed in this paper. As shown in Figure 3, the restriction device is cut from an acrylic plate, and the slide groove on the plate provides applicability for the size of the liver. The scalpel identification frame is made by 3D printing to ensure that the position of the real scalpel is relatively fixed and to synchronize the real scene and the virtual scene. The positioning arm is composed

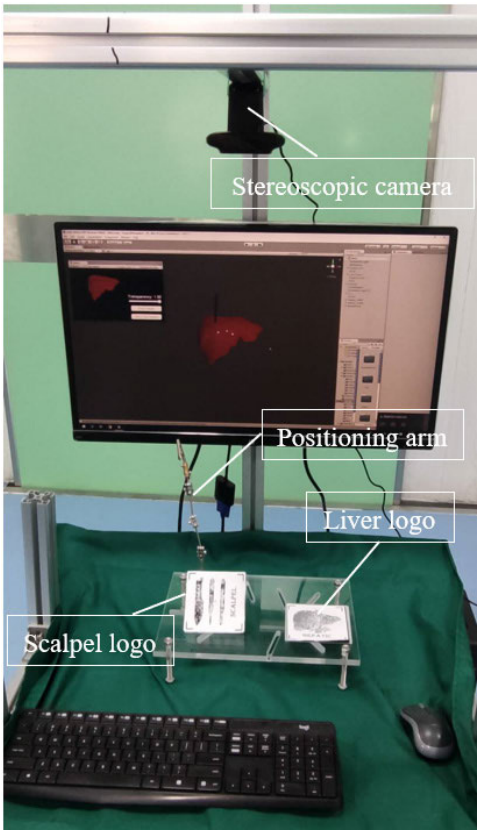

FIGURE 2. Liver model cutting experiment platform.

FIGURE 3. Liver restriction platform.

of four rods and six ball-like hinges to ensure that the position of the liver and the liver mark remains unchanged.

B. SOFTWARE DESIGN

As shown in Figure 4, in order to meet the cutting accuracy and ensure a certain real-time, this paper uses a combination of the surface model and the volume model. The surface model is used to draw the outline of the liver model and the incision during the cutting process, and the volume model is used to calculate the deformation of the model. Due to the poor accuracy of the removal method and the large amount of calculation of the element division method, the cutting part of the surface model uses a progressive moving vertex method different from the removal method and the element

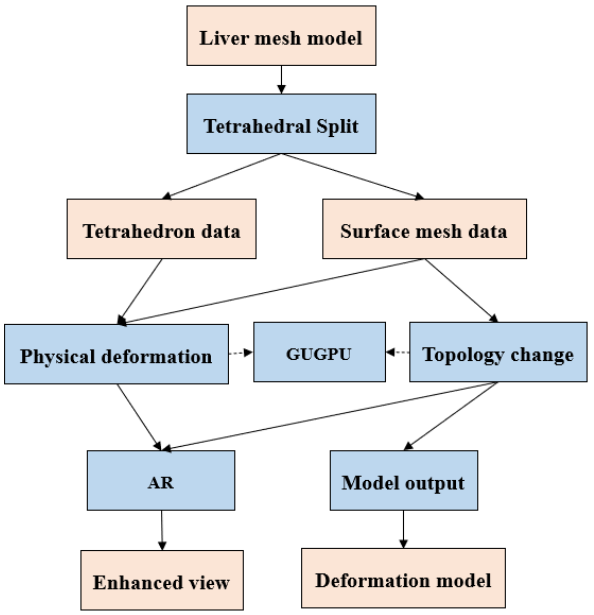

FIGURE 4. Design of liver cutting software.

division method. The moving vertex method was proposed by Nienhuys *et al.* (2001) [25] and Serby *et al.* (2001) [26]. The main idea of this method is moving the vertex closest to the cutting point on the model to the position of the cutting point for each calculation and thus the cutting line can be formed.

1) TOPOLOGICAL CUTTING OF THE SURFACE MODEL BASED ON MOVING VERTEX

The liver surface model cutting mainly includes three procedures: collision detection, model surface mesh cutting, and cutting surface structure. The specific process is shown in Figure 5. First, in order to detect whether the surgical instrument collides with the liver and to obtain the position of the cutting point, collision detection is required. If a collision is detected, the specific position of the collision is calculated, and the collision point is the cutting point, otherwise it's needed to wait for the next collision detection. Then find the nearest point near the cutting point that meets the search conditions. In order to avoid program errors, the nearest points of two adjacent moves cannot be the same vertex. Therefore, when the closest point found is the same as the previous vertex, no processing is performed, and the next collision detection is waited. Otherwise, move the vertex part. In order to eliminate the degenerate triangles generated when moving the vertices, the local mesh is optimized. After that, the moving vertex are duplicated to form a cut. Finally, the cutting surface is structured to form a complete cutting surface.

(a) Collision detection: in order to ensure the normal progress of the cutting, it is a must to first detect whether the surgical instrument model collides with the liver model, and at the same time obtain the collision position, that is, the cutting point. Therefore, collision detection is the basis for all subsequent operations. This paper uses a collision

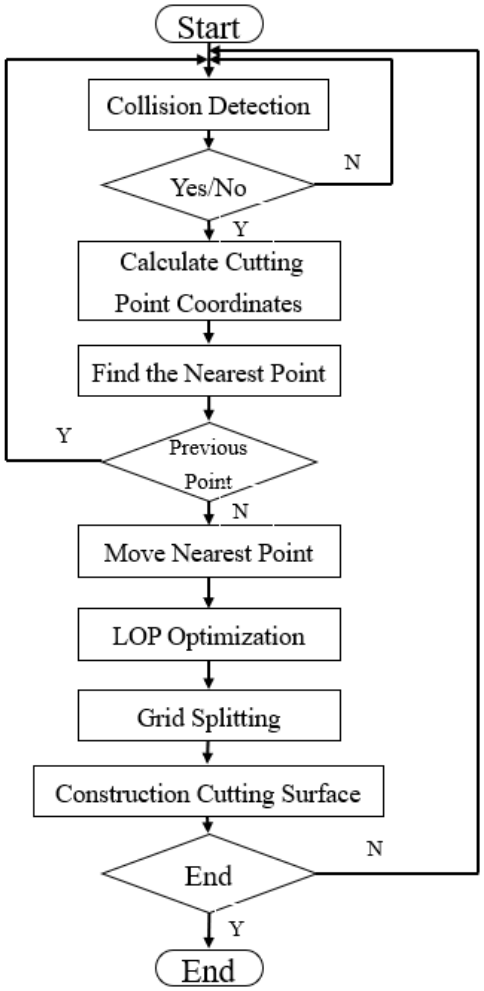

FIGURE 5. Design of liver cutting software.

FIGURE 6. Surgical scalpel.

detection method based on ray projection [27] to render a complete instrument model. But in the process of collision calculation, only the axis has been used. As shown in Figure 6, the two points S_t and S_e are fixed on the surgical blade, and the collision detection calculation is performed using the connection of these two points.

As shown in Figure 7, (1) and (2) are used to calculate the intersection point $P_{c(i)}$ between the line $S_{t(i)}S_{e(i)}$ and the plane where the triangle unit is located. The intersection point is the collision point between the cutter and the liver model.

$$\overrightarrow{P_{c(i)}T_{1(i)}} \cdot \overrightarrow{n_{(i)}} = (T_{1(i)} - P_{c(i)}) \cdot \overrightarrow{n_{(i)}} = 0 \tag{1}$$

$$\begin{aligned} P_{c(i)} &= S_{e(i)} + k_{(i)} \frac{\overrightarrow{S_{e(i)}S_{t(i)}}}{\left|\overrightarrow{S_{e(i)}S_{t(i)}}\right|} \\ &= S_{e(i)} + k_i \frac{S_{t(i)} - S_{e(i)}}{\left|S_{t(i)} - S_{e(i)}\right|} \end{aligned} \tag{2}$$

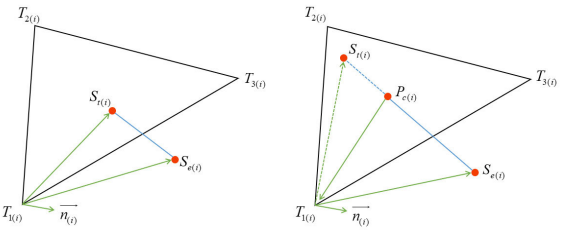

FIGURE 7. Space between scalpel and triangular patch:(a) No collision (b) Collision has occurred.

(b) Surface mesh cutting: it is mainly composed of moving nearest points, Delaunay mesh optimization, copying vertices, and mesh splitting. After the cutting point $P_{c(i)}$ was obtained, the three distance from the triangular points $M_{R(i,j)} = M_{R(i)} + jL_A \frac{\overrightarrow{M_{R(i)}S_{t(i)}}}{\left|\overrightarrow{M_{R(i)}S_{t(i)}}\right|}$ to the cutting point $M_{R(i,j)} = M_{R(i)} + jL_A \frac{\overrightarrow{M_{R(i)}S_{t(i)}}}{\left|\overrightarrow{M_{R(i)}S_{t(i)}}\right|}$ are calculated. And they are sorted in sequence. Then move the vertex closest to point $M_{R(i,j)} = M_{R(i)} + jL_A \frac{\overrightarrow{M_{R(i)}S_{t(i)}}}{\left|\overrightarrow{M_{R(i)}S_{t(i)}}\right|}$ to the position of point $M_{R(i,j)} = M_{R(i)} + jL_A \frac{\overrightarrow{M_{R(i)}S_{t(i)}}}{\left|\overrightarrow{M_{R(i)}S_{t(i)}}\right|}$, that is, modify the coordinates of the nearest point to the coordinates of point $M_{R(i,j)} = M_{R(i)} + jL_A \frac{\overrightarrow{M_{R(i)}S_{t(i)}}}{\left|\overrightarrow{M_{R(i)}S_{t(i)}}\right|}$. Considering the last moved vertex, the normal cutting process is shown in Figure 8. The last moved vertex $M_{R(i,j)} = M_{R(i)} + jL_A \frac{\overrightarrow{M_{R(i)}S_{t(i)}}}{\left|\overrightarrow{M_{R(i)}S_{t(i)}}\right|}$ ($M_{R(i,j)} = M_{R(i)} + jL_A \frac{\overrightarrow{M_{R(i)}S_{t(i)}}}{\left|\overrightarrow{M_{R(i)}S_{t(i)}}\right|}$ in the figure) and the currently moved vertex $M_{R(i,j)} = M_{R(i)} + jL_A \frac{\overrightarrow{M_{R(i)}S_{t(i)}}}{\left|\overrightarrow{M_{R(i)}S_{t(i)}}\right|}$ ($M_{R(i,j)} = M_{R(i)} + jL_A \frac{\overrightarrow{M_{R(i)}S_{t(i)}}}{\left|\overrightarrow{M_{R(i)}S_{t(i)}}\right|}$ in the figure) just form a cutting line along the cutting path. However, when the vertices that are moved twice are diagonal points of a quadrangle, the cutting line along the cutting path cannot be formed normally, and the mesh cannot be split normally in the subsequent mesh splitting step. Therefore, before moving the vertices, this paper uses the data of the previous calculation cycle to add a judgment condition: the previous moving vertex $M_{R(i,j)} = M_{R(i)} + jL_A \frac{\overrightarrow{M_{R(i)}S_{t(i)}}}{\left|\overrightarrow{M_{R(i)}S_{t(i)}}\right|}$ is in the current cutting triangle or the current moving vertex $M_{R(i,j)} = M_{R(i)} + jL_A \frac{\overrightarrow{M_{R(i)}S_{t(i)}}}{\left|\overrightarrow{M_{R(i)}S_{t(i)}}\right|}$ is in the previous cutting triangle. If this condition is met, it means that the vertices which moved twice are in the same triangle unit, and the cutting line can be formed. Otherwise, the triangle where the two cutting points are located must be adjacent triangles. At this time, the moving point can be the second closest point, that is, the point $M_{R(i,j)} = M_{R(i)} + jL_A \frac{\overrightarrow{M_{R(i)}S_{t(i)}}}{\left|\overrightarrow{M_{R(i)}S_{t(i)}}\right|}$ in Figure 9.

During the cutting process, each time a vertex is moved, a narrow and degenerate triangle may be generated. Degenerate triangles will not only reduce the model display quality, but also affect subsequent cutting calculations. Therefore, we must optimize the reconstruction of the

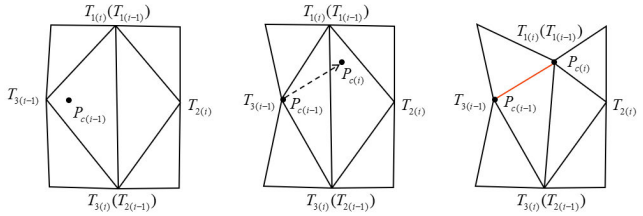

FIGURE 8. Vertex movement process.

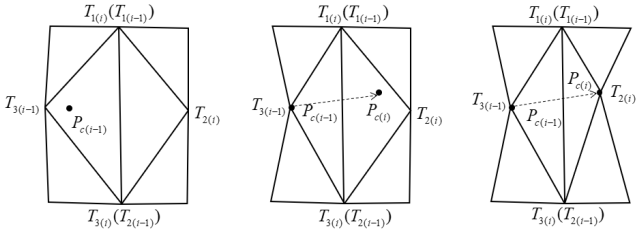

FIGURE 9. Moving a quadrangle cannot form a cutting line.

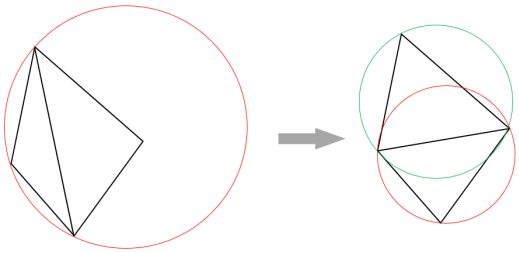

FIGURE 10. LOP optimization process.

degenerate triangle. The liver model used in this paper follows the Delaunay triangulation principle during the reconstruction process [28], so the original liver model does not contain degenerate triangles. Since the method of moving the nearest point used in this paper moves only one vertex at a time, the degenerate triangle must appear in the triangle containing the vertex $M_{R(i,j)} = M_{R(i)} + jL_A \frac{\overrightarrow{M_{R(i)}S_{t(i)}}}{|\overrightarrow{M_{R(i)}S_{t(i)}}|}$, so only the triangle containing the point $M_{R(i,j)} = M_{R(i)} + jL_A \frac{\overrightarrow{M_{R(i)}S_{t(i)}}}{|\overrightarrow{M_{R(i)}S_{t(i)}}|}$ needs to be optimized and reconstructed. This paper uses the Local Optimization Procedure (LOP) to optimize the local grid. The specific method is shown in Figure 10: in two adjacent triangles formed by four vertices, if there is no fourth point in the circumscribed circle of the two triangles, these four points conform to the empty circle characteristic. Otherwise, the diagonals of the quadrilateral can always be exchanged to form two other adjacent triangles so that the two triangles satisfy the empty-circle characteristic and at the same time satisfy the maximum minimum angular characteristic [29].

In order to separate the triangular faces forming the cutting line into cuts, the newly copied vertices need to be moved a certain distance to both sides of the cutting line. The positional relationship between the triangular element and the cutting line can be determined by the method on the left in Figure 11. First, the plane passing through the point

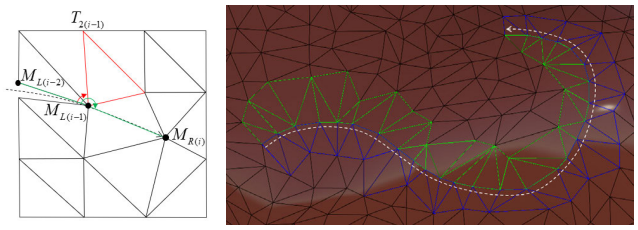

FIGURE 11. Location of triangle unit and cutting line.

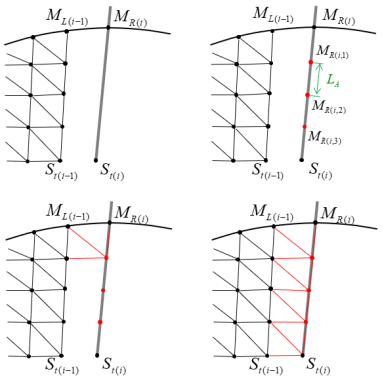

FIGURE 12. Multi-row unit cutting surface structure.

$M_{R(i,j)} = M_{R(i)} + jL_A \frac{\overrightarrow{M_{R(i)}S_{t(i)}}}{|\overrightarrow{M_{R(i)}S_{t(i)}}|}$ and having the same normal vector as the point $M_{R(i,j)} = M_{R(i)} + jL_A \frac{\overrightarrow{M_{R(i)}S_{t(i)}}}{|\overrightarrow{M_{R(i)}S_{t(i)}}|}$ is selected as the reference plane for calculation. Then, taking the plane normal vector as a reference, calculate the clockwise angle $M_{R(i,j)} = M_{R(i)} + jL_A \frac{\overrightarrow{M_{R(i)}S_{t(i)}}}{|\overrightarrow{M_{R(i)}S_{t(i)}}|}$ between the vector $M_{R(i,j)} = M_{R(i)} + jL_A \frac{\overrightarrow{M_{R(i)}S_{t(i)}}}{|\overrightarrow{M_{R(i)}S_{t(i)}}|}$ and the vector $M_{R(i,j)} = M_{R(i)} + jL_A \frac{\overrightarrow{M_{R(i)}S_{t(i)}}}{|\overrightarrow{M_{R(i)}S_{t(i)}}|}$, and the clockwise angle $M_{R(i,j)} = M_{R(i)} + jL_A \frac{\overrightarrow{M_{R(i)}S_{t(i)}}}{|\overrightarrow{M_{R(i)}S_{t(i)}}|}$ between the vector $M_{R(i,j)} = M_{R(i)} + jL_A \frac{\overrightarrow{M_{R(i)}S_{t(i)}}}{|\overrightarrow{M_{R(i)}S_{t(i)}}|}$ and the triangle element clockwise on the first side $M_{R(i,j)} = M_{R(i)} + jL_A \frac{\overrightarrow{M_{R(i)}S_{t(i)}}}{|\overrightarrow{M_{R(i)}S_{t(i)}}|}$. Finally, compare the sizes of the two corners. If $M_{R(i,j)} = M_{R(i)} + jL_A \frac{\overrightarrow{M_{R(i)}S_{t(i)}}}{|\overrightarrow{M_{R(i)}S_{t(i)}}|}$, the triangle unit is on the left side of the cutting line, otherwise the triangle unit is on the right side of the cutting line. The effect of using this method is shown in the right of Figure 11. The triangular elements on the left side of the cutting line are output in green, and the triangular elements on the right side of the cutting line are output in blue.

(c) Construction cutting surface: in order to make the cut more realistic and provide better visual feedback during the augmented reality process, this paper proposes a multi-row triangular element construction method to form a relatively complex curved surface of which the cut element having higher quality. Figure 12 shows the process of cutting surface

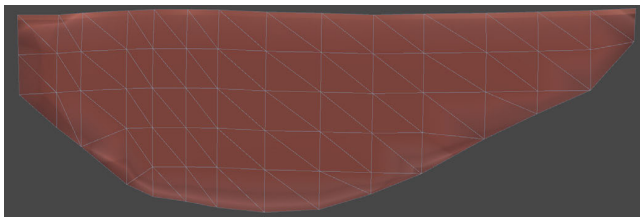

FIGURE 13. Effect of cutting surface.

structure of multiple rows of cells taking the left cutting surface as an example. First, calculate the modulus length of vector $M_{R(i,j)} = M_{R(i)} + jL_A \frac{\overrightarrow{M_{R(i)}S_{t(i)}}}{\left|\overrightarrow{M_{R(i)}S_{t(i)}}\right|}$, which is the distance between point $M_{R(i,j)} = M_{R(i)} + jL_A \frac{\overrightarrow{M_{R(i)}S_{t(i)}}}{\left|\overrightarrow{M_{R(i)}S_{t(i)}}\right|}$ and point $M_{R(i,j)} = M_{R(i)} + jL_A \frac{\overrightarrow{M_{R(i)}S_{t(i)}}}{\left|\overrightarrow{M_{R(i)}S_{t(i)}}\right|}$. Then determine the number of rows $M_{R(i,j)} = M_{R(i)} + jL_A \frac{\overrightarrow{M_{R(i)}S_{t(i)}}}{\left|\overrightarrow{M_{R(i)}S_{t(i)}}\right|}$ of the cutting plane unit. To keep the cutting plane unit consistent with the original model unit, insert a point every $M_{R(i,j)} = M_{R(i)} + jL_A \frac{\overrightarrow{M_{R(i)}S_{t(i)}}}{\left|\overrightarrow{M_{R(i)}S_{t(i)}}\right|}$ distance between the point $M_{R(i,j)} = M_{R(i)} + jL_A \frac{\overrightarrow{M_{R(i)}S_{t(i)}}}{\left|\overrightarrow{M_{R(i)}S_{t(i)}}\right|}$ and the point $M_{R(i,j)} = M_{R(i)} + jL_A \frac{\overrightarrow{M_{R(i)}S_{t(i)}}}{\left|\overrightarrow{M_{R(i)}S_{t(i)}}\right|}$. The point $M_{R(i,j)} = M_{R(i)} + jL_A \frac{\overrightarrow{M_{R(i)}S_{t(i)}}}{\left|\overrightarrow{M_{R(i)}S_{t(i)}}\right|}$ is shared by the left and the right cut surfaces, so it only needs to be inserted once. It is sufficient to insert $M_{R(i,j)} = M_{R(i)} + jL_A \frac{\overrightarrow{M_{R(i)}S_{t(i)}}}{\left|\overrightarrow{M_{R(i)}S_{t(i)}}\right|}$ points between points $M_{R(i,j)} = M_{R(i)} + jL_A \frac{\overrightarrow{M_{R(i)}S_{t(i)}}}{\left|\overrightarrow{M_{R(i)}S_{t(i)}}\right|}$ and $M_{R(i,j)} = M_{R(i)} + jL_A \frac{\overrightarrow{M_{R(i)}S_{t(i)}}}{\left|\overrightarrow{M_{R(i)}S_{t(i)}}\right|}$. Let the inserted points be $M_{R(i,j)} = M_{R(i)} + jL_A \frac{\overrightarrow{M_{R(i)}S_{t(i)}}}{\left|\overrightarrow{M_{R(i)}S_{t(i)}}\right|}$, then the coordinates can be calculated from (3):

$$M_{R(i,j)} = M_{R(i)} + jL_A \frac{\overrightarrow{M_{R(i)}S_{t(i)}}}{\left|\overrightarrow{M_{R(i)}S_{t(i)}}\right|} \tag{3}$$

The effect of the cutting surface is shown in Figure 13.

2) LIVER DEFORMATION MODEL BASED ON MASS SPRING

The accuracy of the simulation of liver deformation largely determines the accuracy of the surgical navigation system [30]. Based on the biomechanical characteristics of liver tissue [31], a mass spring model of liver was established in this paper, and the deformation of the liver model during cutting was simulated and calculated.

The liver model reconstructed by CT is a surface model composed of a triangular mesh. The use of spring damping structures to connect the surface vertices of the model is insufficient to support the liver model to maintain its shape. Therefore, this paper uses Tetgen, an open-source tetrahedral

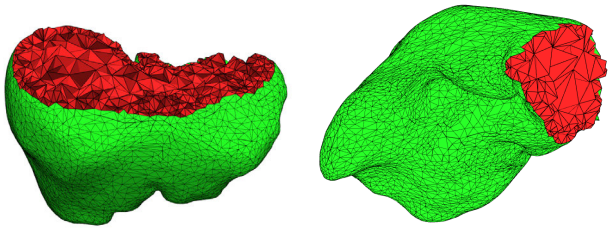

FIGURE 14. Tetrahedral segmentation results of liver model.

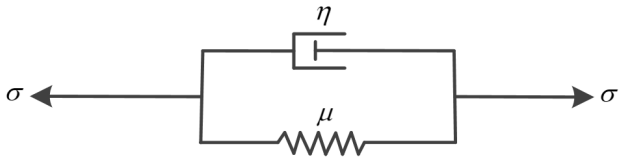

FIGURE 15. Voigt model.

meshing tool, to insert vertices inside the liver model and connect them using a spring damping structure. All vertices participate in physical calculations, and the topological changes and rendering parts are only completed by surface vertices. The effect is shown in Figure 14.

Among the soft tissue characteristics of the liver, viscoelasticity is the most important characteristic during liver deformation. This paper uses the Voigt model [32] to describe the viscoelastic properties of the liver. The Voigt model consists of a spring and a damper connected in parallel, as shown in Figure 15. Use the Voigt element to connect the vertices of the liver model, where each vertex satisfies the following equation:

$$f_{ext(i)} + f_{Voigt(i)} = f_{sum(i)} \tag{4}$$

In (4), $f_{ext(i)} = f_{c(i)} + f_{g(i)} = \Delta s \cdot \overrightarrow{p_i} + m_i \overrightarrow{g}$ is the external force received by the vertex $f_{ext(i)} = f_{c(i)} + f_{g(i)} = \Delta s \cdot \overrightarrow{p_i} + m_i \overrightarrow{g}$, $f_{ext(i)} = f_{c(i)} + f_{g(i)} = \Delta s \cdot \overrightarrow{p_i} + m_i \overrightarrow{g}$ is the force generated by Voigt element at vertex $f_{ext(i)} = f_{c(i)} + f_{g(i)} = \Delta s \cdot \overrightarrow{p_i} + m_i \overrightarrow{g}$, and $f_{ext(i)} = f_{c(i)} + f_{g(i)} = \Delta s \cdot \overrightarrow{p_i} + m_i \overrightarrow{g}$ is the resultant force received by the vertex $f_{ext(i)} = f_{c(i)} + f_{g(i)} = \Delta s \cdot \overrightarrow{p_i} + m_i \overrightarrow{g}$.

The external force on vertex $f_{ext(i)} = f_{c(i)} + f_{g(i)} = \Delta s \cdot \overrightarrow{p_i} + m_i \overrightarrow{g}$ is composed of the interaction force $f_{ext(i)} = f_{c(i)} + f_{g(i)} = \Delta s \cdot \overrightarrow{p_i} + m_i \overrightarrow{g}$ of the surgical instrument and the gravity $f_{ext(i)} = f_{c(i)} + f_{g(i)} = \Delta s \cdot \overrightarrow{p_i} + m_i \overrightarrow{g}$:

$$f_{ext(i)} = f_{c(i)} + f_{g(i)} = \Delta s \cdot \overrightarrow{p_i} + m_i \overrightarrow{g} \tag{5}$$

$\overrightarrow{p_i}$ is the pulling force on vertex i, and Δs is the distance moved by the pulling force.

The force generated by the Voigt element consists of a damping force f_{dmp} and a spring force f_{spr}:

$$\begin{aligned} f_{Voigt(i)} &= \sum_{j \in N_i} (f_{dmp(ij)} + f_{spr(ij)}) \\ &= \sum_{j \in N_i} \left\{ \eta(\overrightarrow{v_i} \cdot \overrightarrow{n_{ij}} - \overrightarrow{v_j} \cdot \overrightarrow{n_{ij}}) + k_{ij}(|r_j - r_i| - |r_j - r_i|_0) \frac{r_j - r_i}{|r_j - r_i|} \right\} \end{aligned} \tag{6}$$

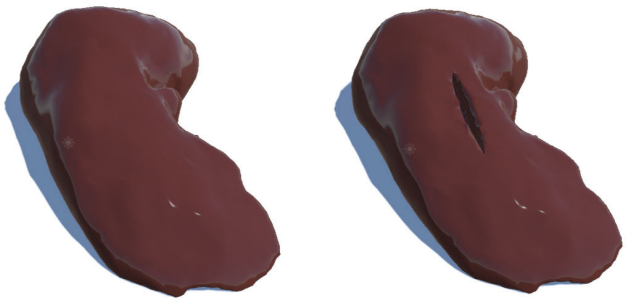

FIGURE 16. Voigt model.

In (6), $\overrightarrow{v}$ is the moving speed of the vertex, $\overrightarrow{r}$ is the space coordinate of the vertex, η is the damping coefficient of the Voigt element connecting vertex i and j, k_{ij} is the stiffness coefficient of the Voigt element connecting vertex i and j, and $\overrightarrow{n_{ij}}$ is the unit direction vector of vertex j pointing to vertex i.

The resultant external force on vertex $f_{sum(i)} = m_i \overrightarrow{a_i}$ is derived from Newton's second law:

$$f_{sum(i)} = m_i \overrightarrow{a_i} \tag{7}$$

Substituting (5), (6), and (7) into (4) can lead to the motion equations for discrete vertex. During the cutting process of the liver model, the liver tissue is regarded as an isotropic structure, that is, $m_i = m$, $\eta_{ij} = \eta$,:

$$\begin{aligned} & m\overrightarrow{a_i} \\ & = \Delta s \cdot \overrightarrow{p_i} + m\overrightarrow{g} \\ & \quad + \sum_{j \in N_i} \left\{ \eta(\overrightarrow{v_i} \cdot \overrightarrow{n_{ij}} - \overrightarrow{v_j} \cdot \overrightarrow{n_{ij}}) + k(|r_j - r_i| - |r_j - r_i|_0) \frac{r_j - r_i}{|r_j - r_i|} \right\} \end{aligned} \tag{8}$$

First calculate the acceleration of the mass according to (8). Then calculate the velocity of the mass at the end of the current calculation cycle:

$$\overrightarrow{v_{i+1}} = \overrightarrow{v_i} + \overrightarrow{\Delta} v = \overrightarrow{v_i} + \overrightarrow{a} \cdot \Delta t \tag{9}$$

Since the increment time Δt of each calculation cycle (about 0.02s) is very short, it can be considered that the particle moves at a constant speed. Therefore, the coordinates of the vertex at the end of the current calculation cycle are:

$$r_{i+1} = r_i + \overrightarrow{v_i} \cdot \Delta t \tag{10}$$

In this way, the positions of all the vertices of the liver model can be obtained in each calculation cycle. The updated liver model can be obtained by updating the surface rendering vertices of the liver model. The cutting effect is shown in Figure 16.

III. EXPERIMENTS

A. AUGMENTED REALITY ERROR ASSESSMENT

In this paper, identification-based augmented reality technology is used. In the process of identifying and tracking the registration, there will be registration errors caused by the loss of data of the identification point. In order to objectively evaluate the accuracy of the designed system, this paper uses the NDI Polaris infrared tracking system to design an augmented reality error measurement scheme and quantify this error. The evaluation platform configuration is shown in Figure 17.

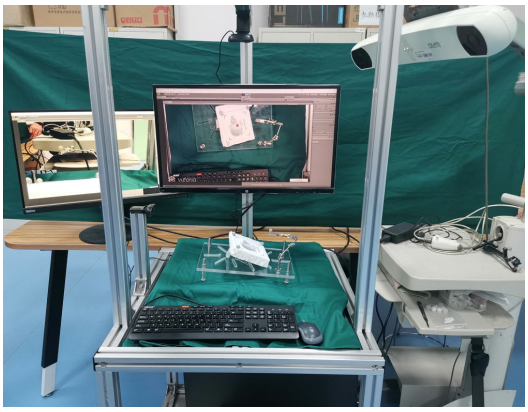

FIGURE 17. Augmented reality system error assessment platform.

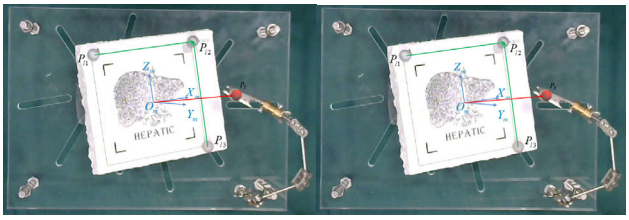

FIGURE 18. Test ball alignment effect in two camera views.

The specific process of error evaluation is: first, fix three mark balls on the identification, and use them as positioning balls to transform the NDI coordinate system to the mark coordinate system. Fix a mark ball on the positioning arm and use it as a test ball to evaluate the error. The identification is divided into a feature area and a positioning area. The interior of the four corner boxes is a feature area for identifying and tracking the augmented reality module. The area between the corner box and the outer square is the positioning area. Subsequently, the identification and the test ball are placed in the NDI measurement range, the coordinates of the three positioning balls and the test ball are read, and a program is written to set the virtual ball position in Unity to the same as the test ball position. Finally, after disturbing the position of the test ball, the reset is continued according to the position of the virtual ball. The difference between two positions read through NDI is the augmented reality error. In the field of view of the depth camera, the test ball alignment effect is shown in Figure 18. In order to ensure the generality of the experiment, this paper conducts experiments on the marker at four different angles, and adjusts and evaluates the test ball position by five different people. The schematic diagram of the four angles is shown in Figure 19.

B. INCISION EVALUSTION OF THE MASS SPRING LIVER MODEL

In order to verify the accuracy of the mass-spring model in simulating the cutting deformation of the liver under the

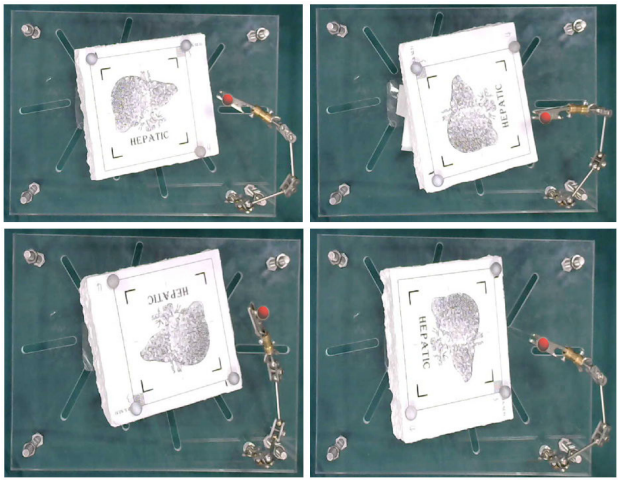

FIGURE 19. Test ball alignment effect in two camera views.

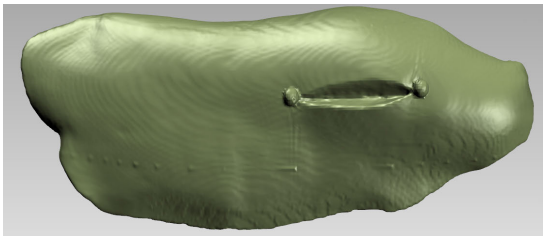

FIGURE 20. Realized model of real gravity cutting of pig liver.

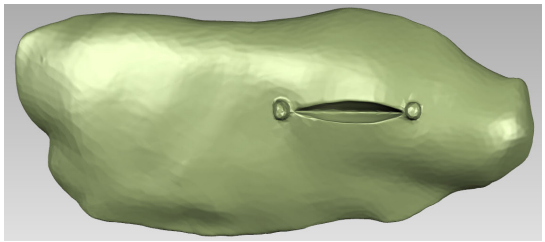

FIGURE 21. Cut model exported and solidified by Unity.

influence of gravity, this paper uses pig livers as the research object to verify. First, place the liver with the cutting starting point on a restricted platform, select PHILIPS BRILLIANCE 64-row / 256-slice spiral CT scanner for plain scan, and import the 3D reconstruction of the film source into Unity as a preoperative model for model cutting. Subsequently, the liver was cut along a preset cutting path to form an incision, and a CT scan was performed again to reconstruct a cutting deformation model of the liver under gravity. Take it as a control group. Finally, the liver preoperative model in Unity was hung on a script, and cut along the same path as the actual cutting. After cutting, the cutting deformation model under Unity was exported as the experimental group. In order to better compare the real model with the virtual model, it is necessary to convert the shell structure of the triangular faceplate into a solid model, as shown in Figures 20 and 21, which are the renderings of the real model and the virtual model.

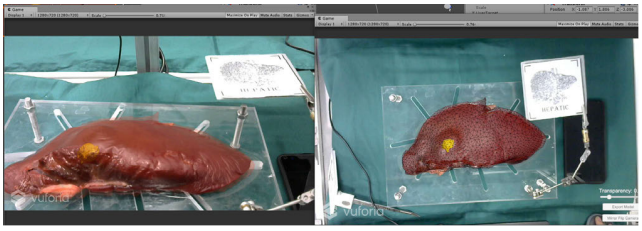

FIGURE 22. Liver registration results.

FIGURE 23. Scalpel registration results.

C. AUGMENTED REALITY-ASSISTED PIG LIVER CUTTING EXPERIMMENT

This experiment integrates all the above experimental content, including 3D reconstruction, augmented reality, cutting deformation under the gravity of the liver, and GPGPU acceleration; simulate the surgical environment of real liver cutting; and complete the circular cutting of internal lesions of pig liver with the aid of AR.

First, put a heterogeneous pellet inside the liver of the pig to represent the tumor. The pellet is of appropriate size and can be separated from the liver parenchyma in CT. The liver is placed on a restricted platform for CT scan. After 3D reconstruction of the data, import it into Unity and set the script. As shown in Figure 22 and 23, the positioning arm is then used to hold the liver mark, and the scalpel and the scalpel mark stand are connected together. Turn on the depth camera to complete the registration of real liver and virtual liver, and real scalpel and virtual scalpel. After the registration is completed, the tumor can be clearly seen inside the liver from the perspective of augmented reality. Finally, the surrounding tumor is cut with the assistance of the augmented reality system. The cutting effect is shown in Figure 24. It can be seen that when the scalpel cuts the real liver, the virtual scalpel is also cutting the liver model synchronously and forming a surrounding cutting line.

IV. EXPERIMENTAL RESULTS AND DISCUSSION

A. AUGMENTED REALITY ERROR RESULTS

Figure 25 shows a total of 20 sets of augmented reality module error evaluation experiments at four different angles. In these 20 sets of experiments, the maximum error of the augmented reality module is 1.99mm, and the minimum value is 1.05mm. The errors at the four angles are 1.54± 0.28mm, 1.77±0.31mm, 1.40±0.30mm, and 1.51±0.24mm, respectively. The average error of this module is 1.55±0.29mm. In addition to the larger average error of the second angle, the other three angle errors are evenly distributed, and the

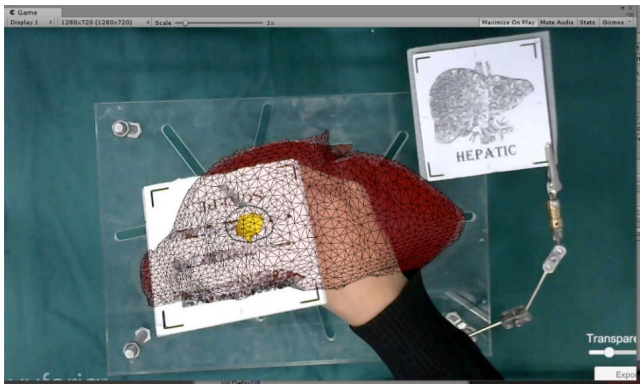

FIGURE 24. Augmented reality surrounding tumor cutting.

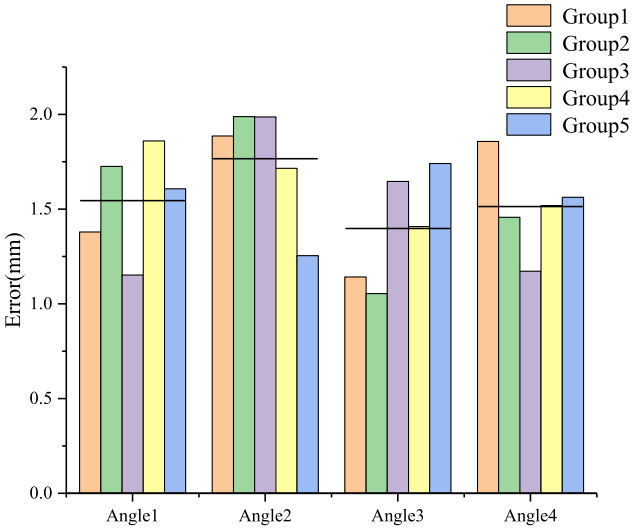

FIGURE 25. Augmented reality error experimental results.

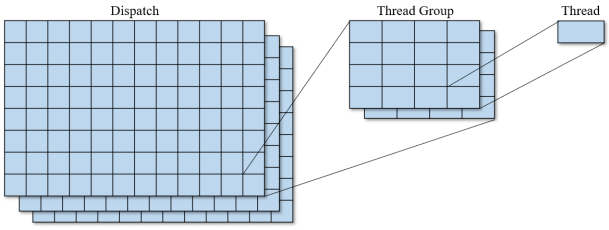

FIGURE 26. Compute Shader thread structure.

four angle errors are within 2mm, which can meet the requirements of liver cutting accuracy [21].

B. GUGPU-BASED PARALLEL COMPUTING ACCELERATION EXPERIMENT RESULTS

The model formed by splitting the triangles into tetrahedrons has 6510 vertices, 24398 tetrahedrons, and 53796 triangles. With the large number of patches, coupled with the complex calculation of the mass spring, the program can not achieve a feeling of smooth results above 30 FPS without parallel calculations [33]. In order to solve the obvious problem of stuttering, this paper uses Computer Shader to implement GUGPU in Unity.

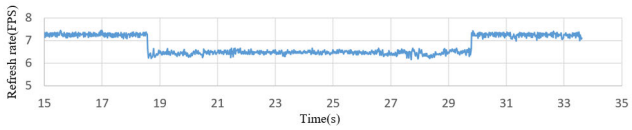

FIGURE 27. Refresh rate of gravity cutting program without GPU acceleration.

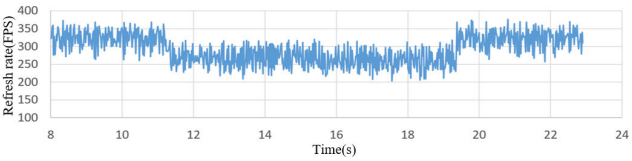

FIGURE 28. Refresh rate of gravity cutting program using GPU acceleration.

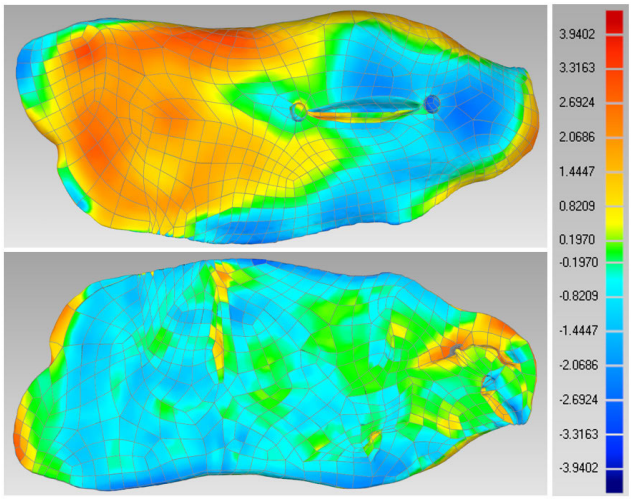

FIGURE 29. Deformation error of pig liver cut under gravity(mm).

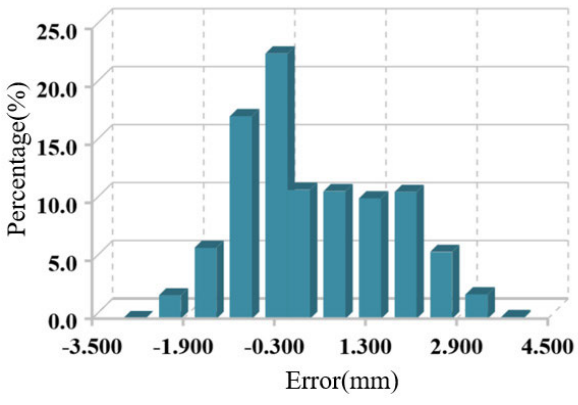

FIGURE 30. Error distribution of cutting deformation.

A task running on the GPU in the Compute Shader is called a Kernel. As shown in Figure 26, threads are divided into three dimensions in the Compute Shader: Dispatch, Thread Group, and Thread. Thread is the unit that runs Kernel. Since the data processed in this paper is basically a one-dimensional array, Dispatch and Numthreads can be set to (20,1,1) and

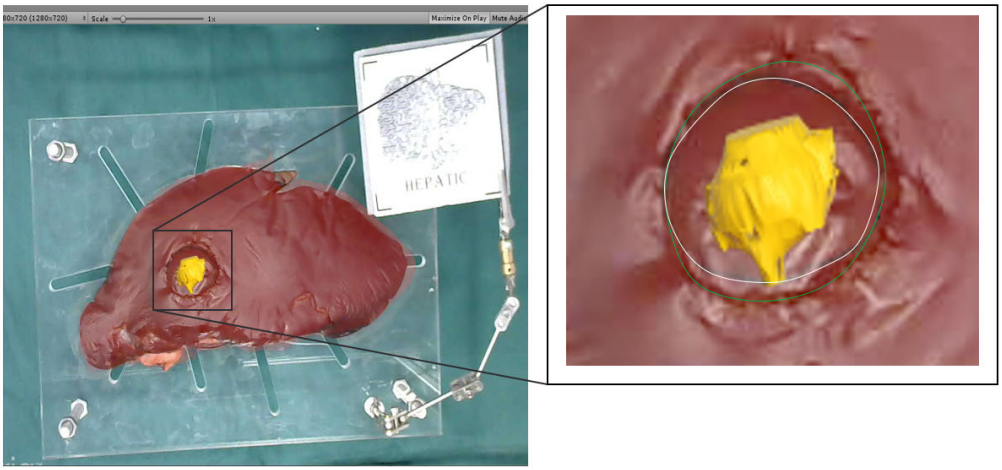

FIGURE 31. Real cutting path and virtual cutting path.

(1024,1,1) respectively. GPU acceleration is used in two places in this paper. One is to find the collision point by topology change. The input data is from the liver model vertex and the tip and the end of the scalpel. The output data is the collision point coordinates and the triangle unit. The other is the calculation part of the mass spring. The input data is the liver model data after the tetrahedral segmentation, and the output data is the liver model vertex coordinates modified by a cutting cycle.

Figure 27 and Figure 28 show the refresh rate of liver cutting experiment under gravity before and after GPU acceleration. In Figure 27, when GPU acceleration is not used, the refresh rate before cutting is around 7.3 FPS, the cutting process is reduced to around 6.5 FPS, and the entire cutting process takes 31 seconds to end. As shown in Figure 28, after the GPU module is turned on, the cutting experiment under gravity is performed again. The whole process takes 22 seconds to complete, and the refresh rate is maintained at 200 FPS or more, which can fully meet the requirements of fluency and real-time performance.

C. INCISION EXPERIMENT RESULTS OF A MASS SPRING LIVER MODEL

The 3D comparison function of Geomagic Quality was used to compare the cutting accuracy of the liver model under the influence of gravity. The real deformation model was set as the reference object, and the virtual model was used as the test object. Figure 29 shows the cutting error of pig liver under the influence of gravity. The upper left corner is the front view and the lower left corner is the bottom view. Because the real deformation model is taken as a reference, a positive error means that the virtual model is outside the real model, and a negative error indicates that the virtual model is inside the real model. It can be seen from the figure that the cutting error is mainly distributed on the front of the cutting. The cut depth of the real model and the virtual model are basically the same. The closer the cut is to the surface, the larger the error. The error of the upper half of the incision is between -2mm and -3mm, and the error is negative overall, indicating

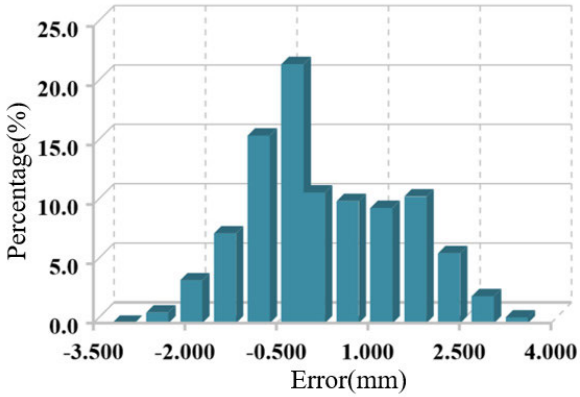

FIGURE 32. Distribution of cutting errors of annular lesions.

that the opening of the virtual incision is larger than the real incision. The error of the lower part of the incision is between 0mm and 3mm, which means that the opening of the virtual incision is smaller than the real incision.

Figure 30 is the histogram of error distribution. It can be seen that most of the errors are distributed between -2mm and 2.5mm, accounting for about 90% of all errors, which can meet the accuracy requirements of the cutting model.

D. AUGMENTED REALITY ASSISTED PIG LIVER CUTTING RESULTS

Figure 31 shows the comparison between the real cutting path and the virtual cutting path, where green is the real cutting path and white is the virtual cutting path. It can be seen that the two paths are in good agreement. Figure 32 is the histogram of the error distribution. As shown in the figure, the error is 0 ± 1.26mm, and the error is mainly distributed between -2mm and 2.5mm, accounting for more than 90% of all errors. The error mainly comes from the tracking module of the augmented reality and the error of the mass spring model. Generally, the error of the surgical assistant system is within 5mm to meet the requirements [21]. Therefore, the error of the augmented reality liver cutting assistant system

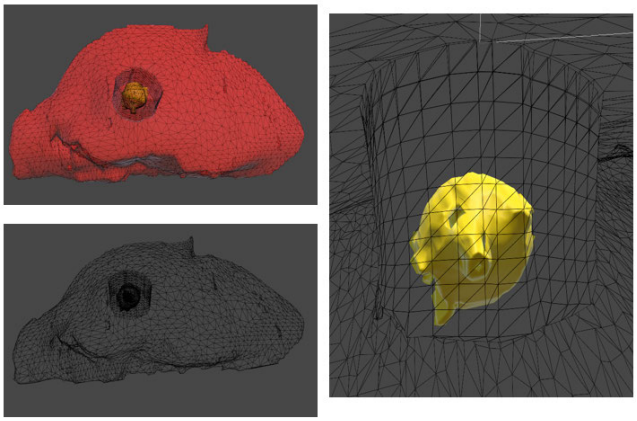

FIGURE 33. Cut surface of a circular lesion.

in this paper when cutting a circular lesion is within an acceptable range.

Adjust the display mode of the cut virtual model. The cutting surface of the circular lesion generated by cutting is shown in Figure 33. The cutting program can form a complete cutting surface in the expected manner, and the cutting depth just reaches the bottom of the lesion.

Intraoperative ultrasound used to detect the location of the tumor originated in 1980s [34], and still plays a huge role in the surgical procedure now. The traditional preoperative CT and intraoperative ultrasound navigation systems need to fully understand the liver anatomy, identify the liver transection line, and then accurately determine the internal liver cut point. Because of the high degree of dependence on doctors' expertise, it is difficult to assess the accuracy of the system. Subsequently, the development of Real-time virtual sonography (RVS) can effectively solve this problem [35]–[37]. However, most current RVS systems require manual registration of CT and ultrasound images. In order to solve the uncertainty caused by manual registration, Takamoto *et al.* (2018) [38] proposed a system of intraoperative ultrasound and preoperative CT real-time registration (less than 20s). 52 patients were selected to verify the feasibility and the accuracy of the system. The results show that the system has a success rate of 83% and an error of more than 1cm. Similar systems can also solve the problem of manual registration, but the common problem is that the accuracy is not satisfactory [37]. Compared with the traditional preoperative CT and the intraoperative ultrasound navigation systems, the augmented reality-based navigation system proposed in this paper has obvious advantages in accuracy and operation complexity.

V. CONCLUSION

In this paper, the feasibility and the key technologies of augmented reality for liver cutting surgery are studied. Modified design of the augmented reality-based liver model cutting program is performed. The liver model is divided into surface mesh and tetrahedron data to complete the functions of surface rendering, topological change and model deformation, and a liver cutting platform under augmented reality is built to realize the basic function of augmented reality assisted liver cutting. Experimental studies were performed on the mass point spring liver model cutting and augmented reality assisted pig liver cutting. The CT scan method was used to compare and verify the deformation of the virtual liver and the deformation of the real liver. The error measurement of the augmented reality module and the image refresh rate were evaluated. Experiments have shown that in terms of real-time performance, the image refresh rate is maintained at 200 FPS or more, which is fully capable of real-time requirements. In terms of accuracy, the error of the augmented reality assist system proposed in this paper can be controlled within 5mm, and it can also meet the accuracy requirements. Therefore, the augmented reality liver cutting assist system proposed in this paper can meet the needs.

However, the surgical navigation system proposed in this paper uses a rigid registration method based on identification. The registration method does not take into account the influence of respiration and other factors on liver deformation. It still requires a lot of effort in clinical trials. Future work will focus on non-rigid registration methods to improve the accuracy of surgical navigation systems.

ABBREVIATION

Augmented reality (AR)
Surgical navigation system (SNS)
Moving cube algorithm (MC)
General Purpose Graphics Processing Unit (GUGPU)
Real-time virtual sonography (RVS)

ACKNOWLEDGMENT

The authors would like to thank the Robotics and Microsystems Control Center, Soochow University.

REFERENCES

[1] G. Torzilli, R. Adam, L. Viganò, K. Imai, J. Goransky, A. Fontana, C. Toso, P. Majno, and E. de Santibañes, "Surgery of colorectal liver metastases: Pushing the limits," *Liver Cancer*, vol. 6, no. 1, pp. 80–89, 2017.

[2] H. G. Kenngott, M. Wagner, M. Gondan, F. Nickel, M. Nolden, A. Fetzer, J. Weitz, L. Fischer, S. Speidel, H.-P. Meinzer, D. Böckler, M. W. Büchler, and B. P. Müller-Stich, "Real-time image guidance in laparoscopic liver surgery: First clinical experience with a guidance system based on intraoperative CT imaging," *Surgical Endoscopy*, vol. 28, no. 3, pp. 933–940, Mar. 2014.

[3] S. Yang, J. Zeng, S. Cai, W. Ji, W. Duan, A. Zhang, W. Ren, Y. Xu, J. Tan, X. Bu, N. Zhang, X. Wang, X. Wang, X. Meng, K. Jiang, W. Gu, Z. Huang, and J. Dong, "Precision in liver surgery," *Seminars Liver Disease*, vol. 33, no. 3, pp. 189–203, Aug. 2013.

[4] J. Hallet, L. Soler, M. Diana, D. Mutter, T. F. Baumert, F. Habersetzer, J. Marescaux, and P. Pessaux, "Trans-thoracic minimally invasive liver resection guided by augmented reality," *J. Amer. College Surgeons*, vol. 220, no. 5, pp. e55–e60, 2015.

[5] J. Marescaux, J.-M. Clément, V. Tassetti, C. Koehl, S. Cotin, Y. Russier, D. Mutter, H. Delingette, and N. Ayache, "Virtual reality applied to hepatic surgery simulation: The next revolution," *Ann. Surg.*, vol. 228, no. 5, pp. 627–634, Nov. 1998.

[6] R. Tang, L.-F. Ma, Z.-X. Rong, M.-D. Li, J.-P. Zeng, X.-D. Wang, H.-E. Liao, and J.-H. Dong, "Augmented reality technology for preoperative planning and intraoperative navigation during hepatobiliary surgery: A review of current methods," *Hepatobiliary Pancreatic Diseases Int.*, vol. 17, no. 2, pp. 101–112, Apr. 2018.

[7] D. W. Roberts, J. W. Strohbehn, J. F. Hatch, W. Murray, and H. Kettenberger, "A frameless stereotaxic integration of computerized tomographic imaging and the operating microscope," *J. Neurosurg.*, vol. 65, no. 4, pp. 545–549, Oct. 1986.

[8] H. J. Marcus, P. Pratt, A. Hughes-Hallett, T. P. Cundy, A. P. Marcus, G.-Z. Yang, A. Darzi, and D. Nandi, "Comparative effectiveness and safety of image guidance systems in surgery: A preclinical randomised study," *Lancet*, vol. 385, p. S64, Feb. 2015.
[9] W. Si, X. Liao, Q. Wang, and P.-A. Heng, "Augmented reality-based personalized virtual operative anatomy for neurosurgical guidance and training," in *Proc. IEEE Conf. Virtual Reality 3D User Interfaces (VR)*, Reutlingen, Germany, Mar. 2018, pp. 683–684.
[10] R. Shirai, X. Chen, K. Sase, S. Komizunai, T. Tsujita, and A. Konno, "AR brain-shift display for computer-assisted neurosurgery," in *Proc. 58th Annu. Conf. Soc. Instrum. Control Eng. Jpn. (SICE)*, Hiroshima, Japan, Sep. 2019, pp. 1113–1118.
[11] J.-D. Lee, H.-K. Wu, and C.-T. Wu, "A projection-based AR system to display brain angiography via stereo vision," in *Proc. IEEE 7th Global Conf. Consum. Electron. (GCCE)*, Nara, Japan, Oct. 2018, pp. 130–131.
[12] N. Navab, S.-M. Heining, and J. Traub, "Camera augmented mobile C-arm (CAMC): Calibration, accuracy study, and clinical applications," *IEEE Trans. Med. Imag.*, vol. 29, no. 7, pp. 1412–1423, Jul. 2010.
[13] N. Navab, S. Wiesner, S. Benhimane, E. Euler, and S. M. Heining, "Visual servoing for intraoperative positioning and repositioning of mobile C-arms," in *Medical Image Computing and Computer-Assisted Intervention*, vol. 9. 2006, pp. 551–560, doi: 10.1007/11866565_68.
[14] A. M. von der Heide, P. Fallavollita, L. Wang, P. Sandner, N. Navab, S. Weidert, and E. Euler, "Camera-augmented mobile C-arm (CamC): A feasibility study of augmented reality imaging in the operating room," *Int. J. Med. Robot. Comput. Assist. Surg.*, vol. 14, no. 2, p. e1885, Apr. 2018.
[15] S. Nicolau, L. Soler, D. Mutter, and J. Marescaux, "Augmented reality in laparoscopic surgical oncology," *Surgical Oncol.*, vol. 20, no. 3, pp. 189–201, Sep. 2011.
[16] N. Tsutsumi, M. Tomikawa, M. Uemura, T. Akahoshi, Y. Nagao, K. Konishi, S. Ieiri, J. Hong, Y. Maehara, and M. Hashizume, "Image-guided laparoscopic surgery in an open MRI operating theater," *Surgical Endoscopy*, vol. 27, no. 6, pp. 2178–2184, Jun. 2013.
[17] F. Cutolo, B. Fida, N. Cattari, and V. Ferrari, "Software framework for customized augmented reality headsets in medicine," *IEEE Access*, vol. 8, pp. 706–720, 2020.
[18] J. Jiang, Z. Huang, W. Qian, Y. Zhang, and Y. Liu, "Registration technology of augmented reality in oral medicine: A review," *IEEE Access*, vol. 7, pp. 53566–53584, 2019.
[19] D. Ntourakis, R. Memeo, L. Soler, J. Marescaux, D. Mutter, and P. Pessaux, "Augmented reality guidance for the resection of missing colorectal liver metastases: An initial experience," *World J. Surg.*, vol. 40, no. 2, pp. 419–426, Feb. 2016.
[20] P. Pessaux, M. Diana, L. Soler, T. Piardi, D. Mutter, and J. Marescaux, "Towards cybernetic surgery: Robotic and augmented reality-assisted liver segmentectomy," *Langenbeck's Arch. Surg.*, vol. 400, no. 3, pp. 381–385, Apr. 2015.
[21] T. Okamoto, S. Onda, M. Matsumoto, T. Gocho, Y. Futagawa, S. Fujioka, K. Yanaga, N. Suzuki, and A. Hattori, "Utility of augmented reality system in hepatobiliary surgery," *J. Hepato-Biliary-Pancreatic Sci.*, vol. 20, no. 2, pp. 249–253, Feb. 2013.
[22] D. C. Rucker, Y. Wu, L. W. Clements, J. E. Ondrake, T. S. Pheiffer, A. L. Simpson, W. R. Jarnagin, and M. I. Miga, "A mechanics-based nonrigid registration method for liver surgery using sparse intraoperative data," *IEEE Trans. Med. Imag.*, vol. 33, no. 1, pp. 147–158, Jan. 2014.
[23] Y. Adagolodjo, N. Golse, E. Vibert, M. De Mathelin, S. Cotin, and H. Courtecuisse, "Marker-based registration for large deformations–application to open liver surgery," in *Proc. IEEE Int. Conf. Robot. Autom. (ICRA)*, May 2018, pp. 1–6.
[24] N. Golse, A. Petit, M. Lewin, E. Vibert, and S. Cotin, "Augmented reality during open liver surgery using a Markerless non-rigid registration system," *J. Gastrointestinal Surg.*, vol. 20, no. 1, pp. 156–163, Feb. 2020, doi: 10.1007/s11605-020-04519-4.
[25] H.-W. Nienhuys and A. F. V. D. Stappen, "A surgery simulation supporting cuts and finite element deformation," in *Medical Image Computing and Computer-Assisted Intervention*, vol. 3. 2001, pp. 145–152.
[26] D. Serby, M. Harders, and G. Székely, "A new approach to cutting into finite element models," in *Medical Image Computing and Computer-Assisted Intervention—MICCAI 2001*, vol. 2208. 2001, pp. 425–433.
[27] C. D. Bruyns, S. Senger, A. Menon, K. Montgomery, S. Wildermuth, and R. Boyle, "A survey of interactive mesh-cutting techniques and a new method for implementing generalized interactive mesh cutting using virtual tools," *J. Visualizat. Comput. Animation*, vol. 13, no. 1, pp. 21–42, 2002.
[28] L. Gao, "Research on improved delaunay triangulation algorithm," M.S. thesis, Dept. Geomatics, Lanzhou Jiaotong Univ., Lanzhou, China, 2015.
[29] C. L. Lawson, "Software for C1 surface interpolation," in *Mathematical Software*. J. R. Rice, Ed. New York, NY, USA: Academic, 1977, pp. 161–194.
[30] L. W. Clements, J. A. Collins, J. A. Weis, A. L. Simpson, L. B. Adams, W. R. Jarnagin, and M. I. Miga, "Evaluation of model-based deformation correction in image-guided liver surgery via tracked intraoperative ultrasound," *J. Med. Imag.*, vol. 3, no. 1, Mar. 2016, Art. no. 015003.
[31] X. R. Zhang, P. P. Wang, W. Sun, J. Liu, and L. F. Zhu, "Research progress of soft tissue cutting model in virtual surgery," *Appl. Res. Comput.*, vol. 34, no. 9, pp. 2561–2569, 2017.
[32] Y. D. Bao, "Experimental research on modeling and cutting of viscoelastic soft tissue and virtual simulation," Ph.D. dissertation, Harbin Inst. Technol., Harbin, China, 2016.
[33] M. Wang and Y. Ma, "A review of virtual cutting methods and technology in deformable objects," *Int. J. Med. Robot. Comput. Assist. Surg.*, vol. 14, no. 5, p. e1923, Oct. 2018.
[34] M. Makuuchi, H. Hasegawa, and S. Yamazaki, "Ultrasonically guided subsegmentectomy," *Surg. Gynecol. Obstetrics*, vol. 161, no. 4, pp. 346–350, 1985.
[35] H. Kawasoe, Y. Eguchi, T. Mizuta, T. Yasutake, I. Ozaki, T. Shimonishi, K. Miyazaki, T. Tamai, A. Kato, S. Kudo, and K. Fujimoto, "Radiofrequency ablation with the real-time virtual sonography system for treating hepatocellular carcinoma difficult to detect by ultrasonography," *J. Clin. Biochem. Nutrition*, vol. 40, no. 1, pp. 66–72, 2007.
[36] L. Sandulescu, A. Saftoiu, D. Dumitrescu, and T. Ciurea, "The role of real-time contrast-enhanced and real-time virtual sonography in the assessment of malignant liver lesions," *J. Gastrointestinal Liver Diseases*, vol. 18, no. 1, p. 103-8, 2009.
[37] S. Satou, T. Aoki, J. Kaneko, Y. Sakamoto, K. Hasegawa, Y. Sugawara, O. Arai, T. Mitake, K. Miura, and N. Kokudo, "Initial experience of intraoperative three-dimensional navigation for liver resection using real-time virtual sonography," *Surgery*, vol. 155, no. 2, pp. 255–262, Feb. 2014.
[38] T. Takamoto, Y. Mise, S. Satou, Y. Kobayashi, K. Miura, A. Saiura, K. Hasegawa, N. Kokudo, and M. Makuuchi, "Feasibility of intraoperative navigation for liver resection using real-time virtual sonography with novel automatic registration system," *World J. Surg.*, vol. 42, no. 3, pp. 841–848, Mar. 2018.

FENGFENG ZHANG (Member, IEEE) received the B.S., M.S., and Ph.D. degrees from the School of Mechanical and Electrical Engineering, Harbin Institute of Technology, in 2001, 2003, and 2009, respectively. He is currently an Associate Professor with the School of Mechanical and Electrical Engineering, Soochow University. He has authored over 30 articles and over eight inventions. His research interests include surgical robot, virtual reality, and biomechanics.

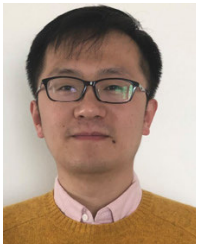

SHI ZHANG is currently a Graduate Student with the College of Mechanical and Electrical Engineering, Harbin Engineering University. His research interests include augmented reality and robot technology.

KAI ZHONG is currently a Graduate Student with the College of Mechanical and Electrical Engineering, Harbin Engineering University. His research interests include surgical robot, augmented reality, and medical image processing.

LINGTAO YU received the B.S., M.S., and Ph.D. degrees in mechanical and electronic engineering from the Harbin Institute of Technology, Harbin, China, in 2000, 2002, and 2007, respectively. From 2014 to 2015, he was a Visiting Scholar with the National University of Singapore. He is currently an Associate Professor with the College of Mechanical and Electrical Engineering, Harbin Engineering University. His research interests include medical robotics, artificial intelligence and robotics, parallel robot, machine learning, machine vision, and biomechanics.

LI NING SUN is currently the Director of the Robotics and Microsystems Center and the President of the College of Mechatronic Engineering, Soochow University. He has more than 300 academic articles being published and more than 20 patents of invention being authorized. His current research interests include micronano operational robot and equipment, advanced robot and control, and electromechanical integration equipment. He received the China National Funds for Distinguished Young Scientists, the two National Science and Technology Awards Grade II, and the three Provincial Science and Technology Prizes Grade I.